

Formation of free round jets with long laminar regions at large Reynolds numbers

Julia Zayko, Sergey Teplodvskii, Anastasia Chicherina, Vasily Vedeneev, and Alexander Reshmin

Citation: *Physics of Fluids* **30**, 043603 (2018); doi: 10.1063/1.5021017

View online: <https://doi.org/10.1063/1.5021017>

View Table of Contents: <http://aip.scitation.org/toc/phf/30/4>

Published by the *American Institute of Physics*



**COMPLETELY
REDESIGNED!**

**PHYSICS
TODAY**

Physics Today Buyer's Guide
Search with a purpose.

Formation of free round jets with long laminar regions at large Reynolds numbers

Julia Zayko, Sergey Teplovodskii, Anastasia Chicherina, Vasily Vedenev, and Alexander Reshmin

Institute of Mechanics, Lomonosov Moscow State University, Moscow, Russia

(Received 30 December 2017; accepted 16 March 2018; published online 6 April 2018)

The paper describes a new, simple method for the formation of free round jets with long laminar regions by a jet-forming device of ~ 1.5 jet diameters in size. Submerged jets of 0.12 m diameter at Reynolds numbers of 2000–12 560 are experimentally studied. It is shown that for the optimal regime, the laminar region length reaches 5.5 diameters for Reynolds number $\sim 10\,000$ which is not achievable for other methods of laminar jet formation. To explain the existence of the optimal regime, a steady flow calculation in the forming unit and a stability analysis of outgoing jet velocity profiles are conducted. The shortening of the laminar regions, compared with the optimal regime, is explained by the higher incoming turbulence level for lower velocities and by the increase of perturbation growth rates for larger velocities. The initial laminar regions of free jets can be used for organising air curtains for the protection of objects in medicine and technologies by creating the air field with desired properties not mixed with ambient air. Free jets with long laminar regions can also be used for detailed studies of perturbation growth and transition to turbulence in round jets. *Published by AIP Publishing.* <https://doi.org/10.1063/1.5021017>

I. INTRODUCTION

Free jets and other shear flows often occur in nature and various technologies and are widely studied. Turbulent jets and their breakdown have been thoroughly studied over several decades in the context of many industrial applications, including mixing, combustion, noise generation, and others.^{1,2,6,8,9,18,22,25,29,30,43,45}

Laminar jets are studied much less because of their immediate breakdown in normal conditions. If created, the laminar initial regions of free jets of sufficient length could be used to organise air curtains, which provide zones of clean air not mixed with the ambient medium. Local clean zones can be used in medicine, medical industry, microelectronics, and other technological processes. The main impediment to the creation of jets with long laminar regions at high Reynolds numbers is their instability, which results in the turbulisation of the flow, typically occurring at the distance of the order of the jet diameter from the orifice. Sections I A and I B give a brief state-of-the-art review of round jet stability and experimental methods of producing laminar jets. Extensive reviews of subsonic jet stability are given by Michalke,³² Morris,³⁵ and Grek *et al.*¹⁴

A. Studies of jet stability

The necessary instability condition of a unidirectional round jet of the inviscid fluid has the following form:³⁸ the expression

$$Q(r) = \frac{ru'}{n^2 + \alpha^2 r^2} \quad (1)$$

should have a numerical maximum in some point of the flow; this condition is generalisation of the inflection-point instability condition for planar flows to axisymmetric flows. In (1), n

and α are azimuthal and axial wavenumbers of the Fourier component of the disturbance, respectively, u is the mean velocity, and r is the radial coordinate. Later, Batchelor and Gill⁴ generalised Fjørtoft's condition¹² and Howard's semicircular theorem¹⁶ to axisymmetric shear flows. As typical examples, they examined round jets of a "top-hat" profile, which represents a jet near the orifice (including its limit form of cylindrical vortex sheet), and a self-similar "far-downstream" profile.²⁴ For the "top-hat" profile, eigenmodes with numerous (but finite-amount) n are growing (all n are growing for the limit case of a cylindrical vortex sheet). For the "far-downstream" profile, only helical sinuous modes ($n = 1$) are growing.⁴

For viscous perturbations of the "far-downstream" profile, all axisymmetric disturbances, $n = 0$, are damped, whereas for $n = 1$, the critical Reynolds number is 37.6, that is, very small.³⁴ For the parabolic jet profile, the axisymmetric perturbations, $n = 0$, are also damped, and for helical perturbations, $Re_{cr} = 32.8$ and 171 for $n = 1$ and 2, respectively.¹⁹ All these results are obtained in a parallel-flow approximation which is not valid for such low Reynolds numbers, so it can only be concluded that for larger Re , where the jet flow is close to unidirectional, the jet is unstable.

If the parallel-flow approximation is not used,⁴² Re_{cr} for a helical mode with $n = 1$ of the "far-downstream" profile drops from 37.6 to 28.4. However, a more surprising result is that the axisymmetric mode $n = 0$, which is damped in parallel-flow approximation, grows, and its $Re_{cr} = 15.0$ is even less than for the helical mode.

Calculations of the absolute instability boundary of jet flows show that free jets of incompressible fluid are always convectively unstable, at least in parallel-flow approximation.³³ This result explains the existence of sufficiently long

laminar portions of jets at $Re > Re_{cr}$ in many experimental studies (Sec. I B).

Numerous recent studies are devoted to the governing of submerged jets and the suppression of turbulence in free shear layers of such jets.^{14,17,46} A few of them are devoted to the development of perturbations^{20,23} in free jets. In the context of this paper, two studies can be especially mentioned. First, Cohen and Wygnanski⁷ theoretically and experimentally studied perturbation growth near the orifice, where the jet profile is “top-hat.” Perturbations with $n = 0$ and 1 demonstrate a good agreement between experiment and linear inviscid stability analysis. Second, Kozlov *et al.*²³ studied round jets flowing from a round pipe, with various incoming conditions and pipe lengths. They showed that the longer laminar portion of a jet was obtained with longer pipes, and the longest result was obtained with the parabolic profile’s formation at the pipe outlet.

B. Experimental methods of creating laminar jets

Because of extremely small Re_{cr} for jets, their laminar region lengths are determined by the flow characteristics at the outlet of the jet-forming device, that is, by the velocity profile, which is responsible for linear perturbation growth rates, and the intensity of turbulence, which is responsible for the initial amplitudes of the perturbations.

To obtain round laminar jets, the most popular method uses laminar pipe flow, as shown in Fig. 1(a). Viilu⁴⁴ used pipes of diameters varying from 0.46 to 1.32 mm. Its length-to-diameter ratio exceeded 50 to produce the parabolic Poiseuille profile at the pipe outlet. The experimental Re_{cr} obtained was between 10.5 and 11.8 (hereafter, for consistency, the Reynolds number is always based on the orifice diameter and average velocity, even if the authors of the cited papers used different definitions). McNaughton and Sinclair³¹ experimentally studied liquid-into-liquid jets in short cylindrical vessels using a pipe with the length-to-diameter ratio of 40 for the jet of the diameter 1”. The maximum length of the laminar region was 18” at the Reynolds number in the pipe of 800. For $Re \geq 3000$, the jet was fully turbulent. A similar scheme

[Fig. 1(a)] was used by Kozlov *et al.*²³ Large-scale vortical structures coming from the fan blades were broken, and the flow was laminarised by passing through the honeycomb and grids into the antechamber of the jet-forming device. At the nozzle exit, a laminar jet is formed in a certain range of Reynolds numbers. Then this jet enters a long smooth cylindrical pipe of diameter $D = 0.02$ m. The transition to turbulence in the pipe does not occur if the turbulence intensity of an incoming jet is sufficiently low. The Poiseuille parabolic velocity profile was obtained²³ for the Reynolds number 6667 for the pipe length $200D$. The forming of the Poiseuille profile at the pipe end leads to a transition to turbulence in the free jet at a distance of $10D$. Laminar pipe flows were also used to create laminar jets by many other authors.^{3,26,41} To some extent, the work of Koller-Milojević and Schneider²¹ can also be related to this method, although their “conventional nozzle” was quite short.

While efficient for narrow jets and low Reynolds numbers, this method has a significant disadvantage when scaled to wider jets. The velocity profile, which differs from the Poiseuille profile by less than 1%, is formed in the pipe of the diameter D at the length³⁷ $l = 0.065 \cdot D \cdot Re$. This explains why only small-scale jets can be produced in this way; say, to form a laminar jet with the diameter of 0.1 m at $Re = 3000$, the pipe length of the order of 20 m would be required.

Another method was used in experiments devoted to the transition to turbulence in coaxial jets by Navoznov *et al.*³⁶ They used honeycombs made of thin tubes of variable lengths [Fig. 1(b)] to form an internal round jet with a velocity profile independent of the turbulence level. A metal grid was installed at the outlet of the forming device, such that the turbulence intensity downstream from the grid was less than 1%. They obtained the laminar jet length of $20D$ for $Re = 1300$ and $9D$ for $Re = 2700$ with the jet diameter of 0.028 m. Therefore, this method of forming the velocity profile with low turbulence intensity by honeycombs and a covering grid is effective and could be scaled to wider jets; however, the production of honeycombs of inconstant lengths and the maintenance of the device are quite laborious. Note that a similar technique, namely, a honeycomb covered by a metal grid, was used in the experiments of Liang and Maxworthy²⁷ but with another goal, namely, to generate swirling jets.

C. The goal of this study

As shown, the main impediments to the generation of round laminar jets of sufficiently large diameters and length-to-diameter ratios are the huge length of the pipe in the first method and the complexity of the jet-forming device in the second. In this study, we present a new, simple method for the formation of free laminar jets with the diameter $D = 0.12$ m, that is, by an order wider than is accessible for other methods. The transition to turbulence occurs at a distance of $5.5D$ from the orifice, while the size of the forming device is only $\sim 1.5D$. The device design is based on the studies of Navoznov *et al.*³⁶ and Reshmin *et al.*,⁴⁰ where a similar type of device was used to study turbulent flows. Namely, it was experimentally found that a short diffuser covered by a grid significantly reduces total pressure loss in turbulent flows in suddenly expanding

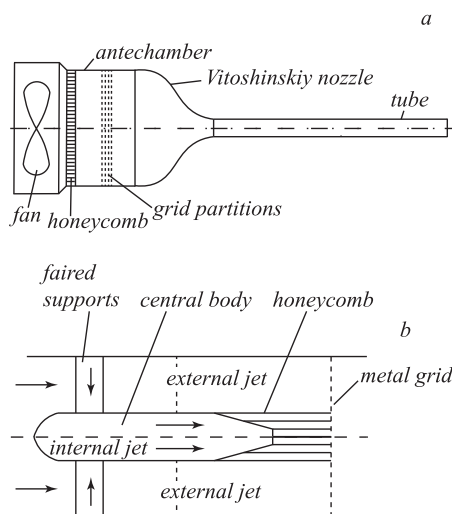


FIG. 1. Experimental device for creating (a) a round jet²³ and (b) coaxial jets.³⁶

channels. However, no attempts to produce laminar jets were made by those authors.

The structure of the paper is as follows. In Sec. II, we describe the jet generation method and the experimental apparatus used to conduct measurements. Section III is devoted to the design of the jet-forming unit. Next, Sec. IV presents the results of experimental studies, including the lengths of laminar portions of jets obtained at various regimes. To explain these results, the rest of the paper is devoted to the theoretical analysis of the flow. Section V is devoted to the detailed numerical modeling of the steady flow in the jet-forming unit and the link between the jet profile and the flow structure inside the device. In Sec. VI, we conduct an inviscid instability analysis of jet profiles and explain the existence of the optimal jet generation regime corresponding to the jet's longest laminar portion. Finally, in Sec. VII, we compare our results with other studies in terms of laminar jet length and summarise this study's results.

II. EXPERIMENTAL METHODS AND CONDITIONS

The experimental apparatus consists of the air supply device (pipeline), the forming device, and the measurement system. The forming device's picture and the scheme are shown in Fig. 2. Air flows from the gasholder to the forming device via a pipeline (1). Then it enters the forming device's first section through a short pipe. This section is a cylindrical channel of 0.04 m in diameter, where the flow is smoothed passing through a perforated plate (2) which also reduces the spatial scale of turbulent fluctuations. After the plate, the flow passes through a bushing with metal grids (3) of 0.05 m in length which is located at a distance of 0.03 m downstream from the perforated plate which reduces turbulence level. The second section of the forming device (short diffuser) is located at a distance of 0.06 m downstream from the bushing. At a length of 0.04 m, the flow expands to a diameter of 0.12 m through the diffuser (4) from which the jet flows to the atmosphere. For low incoming turbulence, the diffuser wall shape and the grid package (5) at the diffuser outlet provide low outgoing turbulence and the jet profile with almost constant velocity at the central jet core of 0.05 m in diameter.

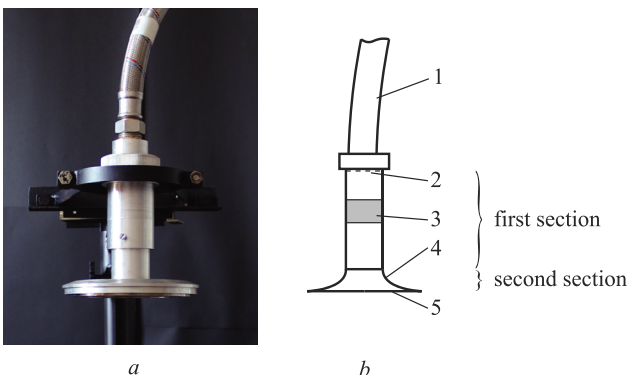


FIG. 2. The photograph (a) and the scheme (b) of the forming device. The pipeline from the gasholder (1), the perforated plate (2), the bushing with metal grids (3), the short diffuser (4), and the grid package (5).

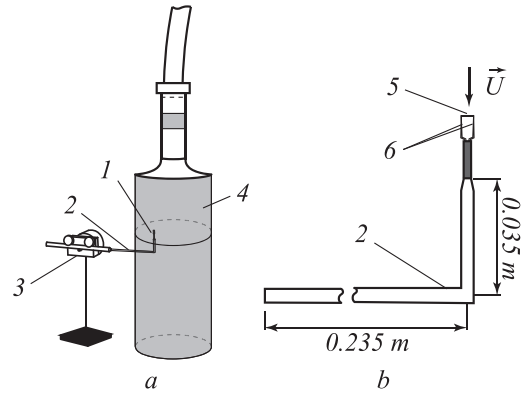


FIG. 3. The scheme of the measurement system (a) and the orientation of the sensor in the flow (b). Probe (1), probe support (2), traversing mechanism (3), jet (4), sensor: thin wire (5), and prongs (6).

Thermoanemometer DISA 56C01 CTA is used for the velocity measurements. The signal is transferred to the analogue-digital converter connected to a personal computer. The velocity is measured by small-sized probes Dantec Dynamics 55P11. The probe has a wire sensor mounted on two straight needle-shaped prongs. The wire is 1.25 mm long and 5 μm thick. The anemometer's probe is mounted on the probe support and then is placed into the flow with the wire perpendicular and the prongs parallel to the flow (Fig. 3). The probes are calibrated in a standard way. The traversing apparatus is used to move the probe in the jet cross sections so that the velocity versus radial coordinate is measured. The disturbance of the flow produced by the probe is negligible due to small sensor size. The effect of the probe support on the upstream flow field (where the sensor is located) is also minor due to the position of the probe support.

The jet visualisation system is shown in Fig. 4. It consists of laser KLM-532 (1) and video camera Bonito CL-400B (2). Light-reflecting particles are generated at the aerosol generator (3) and introduced to the flow through a hose (4). A segment of the jet is illuminated by the laser light sheet (5). The image is taken by the camera, whose optical axis is normal to the plane of the laser light sheet.

The Particle Image Velocimetry (PIV) measurements are obtained through the Polis PIV system, consisting of the same

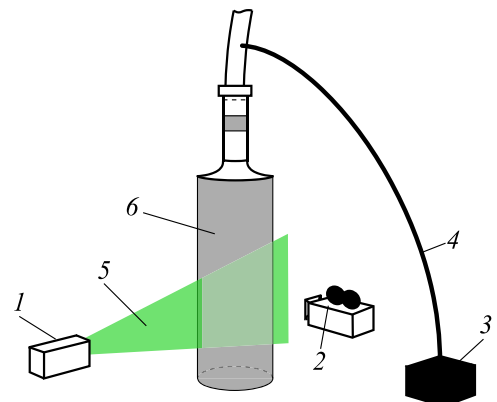


FIG. 4. The scheme of the visualisation system. Laser (1), video camera (2), aerosol generator (3), hose (4), laser light sheet (5), and jet (6).

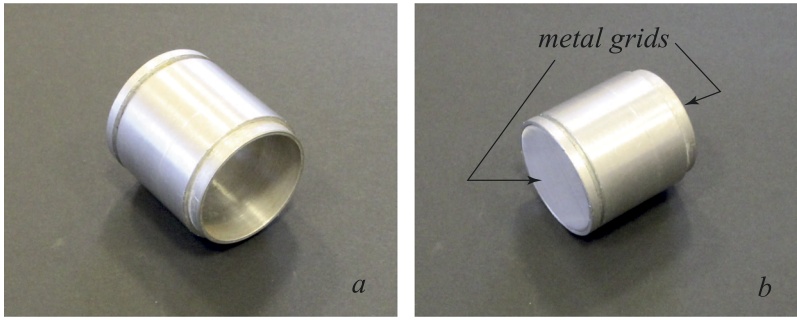


FIG. 5. Bushing without (a) and with (b) metal grids.



FIG. 6. Short diffuser without (a) and with the metal grid package at the outlet (b) and the scheme of short diffuser (c).

camera, aerosol generator, and impulse laser Beamtech Vlithi-100. The system provides the temporal resolution of up to 100 vector fields per second.

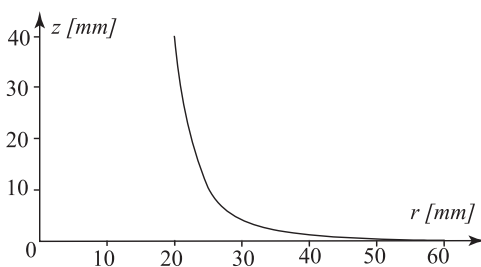
III. THE FORMING DEVICE

A. The inlet section

To form the laminar jet, it is necessary to suppress turbulent fluctuations in the incoming flow. The first section of the device is a cylindrical channel of 0.04 m in diameter and 0.14 m in length. The perforated grid plate with 0.6 mm diameter holes and a holes-to-plate area ratio of 0.8 is placed in the cylindrical channel inlet. A cloth of dense texture is installed before the perforated plate. The bushing of 0.05 m in length with metal grids (Fig. 5) is placed at a distance of 0.03 m downstream from the perforated plate. The measurements show that the resulting flow after the first section is laminar and that the intensity of turbulent fluctuations is less than 0.6%.

B. The outlet section

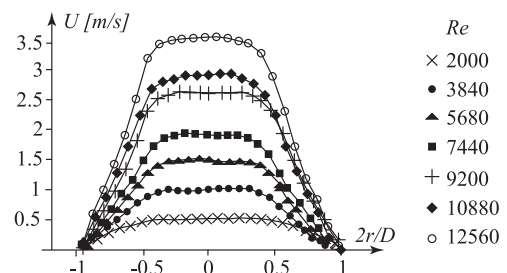
The outlet section of the forming device is a short diffuser (Fig. 6). The outlet-to-inlet diameter ratio D_2/D_1 of the diffuser is 3. Its channel length is equal to the inlet diameter. The diffuser wall profile is shown in Fig. 7. The attached flow

FIG. 7. The profile of the diffuser wall; the z axis is directed upwind.

can exist in the expanding conical channel if the expansion angle does not exceed 12° – 14° .¹⁰ For larger angles, the flow separates from the wall, and a considerable growth of turbulent fluctuations is observed. To prevent separation from the diffuser's suddenly expanding channel, we add a package of two metal grids (Fig. 2, 5) which consists of the brass grid (wire diameter is 0.05 ± 0.004 mm; free area ratio is 34.4%) and the stainless steel grid (wire diameter is 0.03 ± 0.004 mm; free area ratio is 32.7%). The grids constrain the flow and cause its expansion in the radial direction without significant separation. The simultaneous action of the grid package and certain wall shape provides no reverse flow in the diffuser, and only a relatively small local laminar separation occurs for some velocity regimes which is confirmed by the numerical calculations presented in Sec. V.

IV. EXPERIMENTAL RESULTS

Measurements of the velocity profile along the diffuser diameter in different directions show that the velocity distribution at the outlet section is approximately symmetric to the channel axis and depends only on the radial coordinate r . Figures 8 and 9 show mean velocity profiles and velocity

FIG. 8. Mean velocity profiles at a distance of 5 mm from the outlet section (outlet package of two metal grids) of the diffuser. U is mean velocity and r is the radial coordinate.

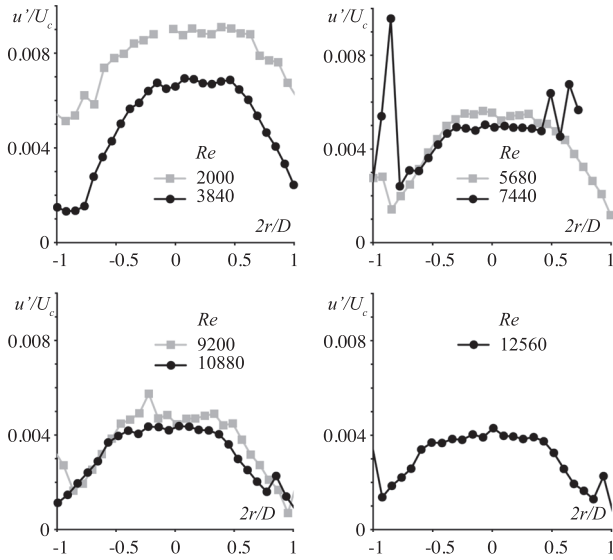


FIG. 9. Turbulent velocity fluctuations at a distance of 5 mm from the orifice (package of two metal grids) of the diffuser.

fluctuations, respectively, at a distance of 5 mm downstream from the outlet section (i.e., outlet package of two metal grids) of the diffuser. The results are shown for various Reynolds numbers $Re = \rho U_{av} D / \mu$, where $\rho = 1.2 \text{ kg/m}^3$ is the air density, U_{av} is the velocity averaged over the cross section, $D = 0.12 \text{ m}$ is the outlet diameter of the diffuser, and $\mu = 1.79 \times 10^{-5} \text{ Pa s}$ is the dynamic viscosity of the air. The list of the regimes studied is shown in Table I, where U_c is the velocity at the jet axis.

During the first series of tests, the mean velocity and velocity fluctuations are measured by a thermoanemometer at the jet axis at different distances downstream from the diffuser outlet with a step of 0.12 m. Measurements at the fixed regime show that the velocity and intensity of turbulent fluctuations at the jet axis remain constant at a distance of several (1-6, depending on the regime) outlet diffuser diameters and farther downstream start to change: the mean velocity decreases and the turbulent fluctuations increase. Then the region of the change was passed with a smaller step of 0.06 m. Figure 10 shows the results of these tests for various velocity regimes. It is seen that the longest laminar region at the jet axis is obtained in the range of $Re = 5680\text{--}9200$. As the transition to turbulence usually starts near the jet boundary, where the shear layer has the inflection point, measurements along

TABLE I. Maximum velocity U_c , average velocity U_{av} , and corresponding Reynolds number of the studied jets.

U_c (m/s)	U_{av} (m/s)	Re
0.5	0.25	2000
1.0	0.48	3840
1.5	0.71	5680
2.0	0.92	7440
2.5	1.14	9200
3.0	1.35	10880
3.5	1.56	12560

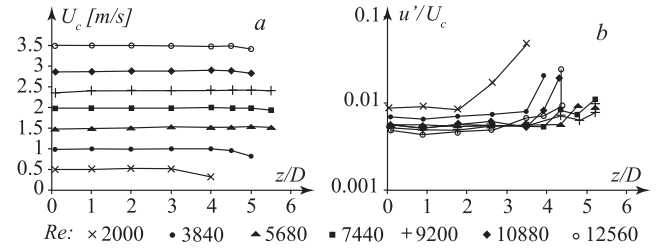


FIG. 10. Mean velocity U (a) and velocity fluctuations u'/U (b) at the jet axis. z is the coordinate along the jet axis, $z = 0$ at the diffuser outlet.

the jet axis give a score from above of the fully laminar jet length.

The second series of experiments is devoted to the careful measurement of the laminar jet length at the same regimes. The velocity and turbulent fluctuation profiles in cross sections of the jet are measured with a step of one diffuser outlet diameter $D = 0.12 \text{ m}$ along the jet axis. Observations of the visualized jet (such as shown in Fig. 15), PIV, and hot-wire anemometer measurements show that the jet stays laminar while the velocity fluctuations do not exceed 14%, which is why this level of fluctuation was taken as a criterion of the jet laminarity. To illustrate this threshold, Fig. 11 shows the level of velocity fluctuations (right figures) for three jet states: laminar, transition (formation of vortex rings is seen), and fully turbulent. It is seen that for the laminar jet the velocity fluctuations do not exceed 1%–5% in the jet core and 14% in the shear layers, whereas for other jet states they grow at least up to 25%–30%. According to this criterion, the maximum distance from the diffuser outlet at which the mean velocity profiles change negligibly and velocity fluctuations are less than 14% is determined for each regime. We call this distance the length of the jet laminar region. Figure 12 shows the profiles of the turbulent fluctuations measured by the thermoanemometer at the maximum distance L_{lam} , where the jet is laminar, and $L_{lam} + D/2$, where the start of transition is seen (turbulent fluctuations increase and exceed 14%). Figure 13 shows the mean velocity profiles at the same distances from the diffuser outlet, where increasing deformation of the profile near the jet boundary is seen. Based on the results of the second series of tests, we conclude that the length of the jet laminar region is maximum for $Re = 7440\text{--}9200$ and is equal to $5.5D$ (Fig. 14).

Figure 9 shows that the initial turbulent fluctuations are higher for the first three regimes compared with the other regimes. Therefore, we conclude that the higher level of incoming turbulence is responsible for the shorter laminar region for these regimes comparing with $Re = 7440$ and 9200 . The reason for the shorter laminar region for $Re \geq 10880$ is the higher growth rates of small perturbations, as will be discussed in Sec. VI.

The third series of experiments is devoted to the visualisation of the jet at different velocity regimes. The aerosol generator and the visualisation method are described in Sec. II. Figure 15 shows an example of the visualised jet with a long laminar region at $Re = 7240$ (a) and the jet breaking down near the diffuser outlet (b). Visualisation results

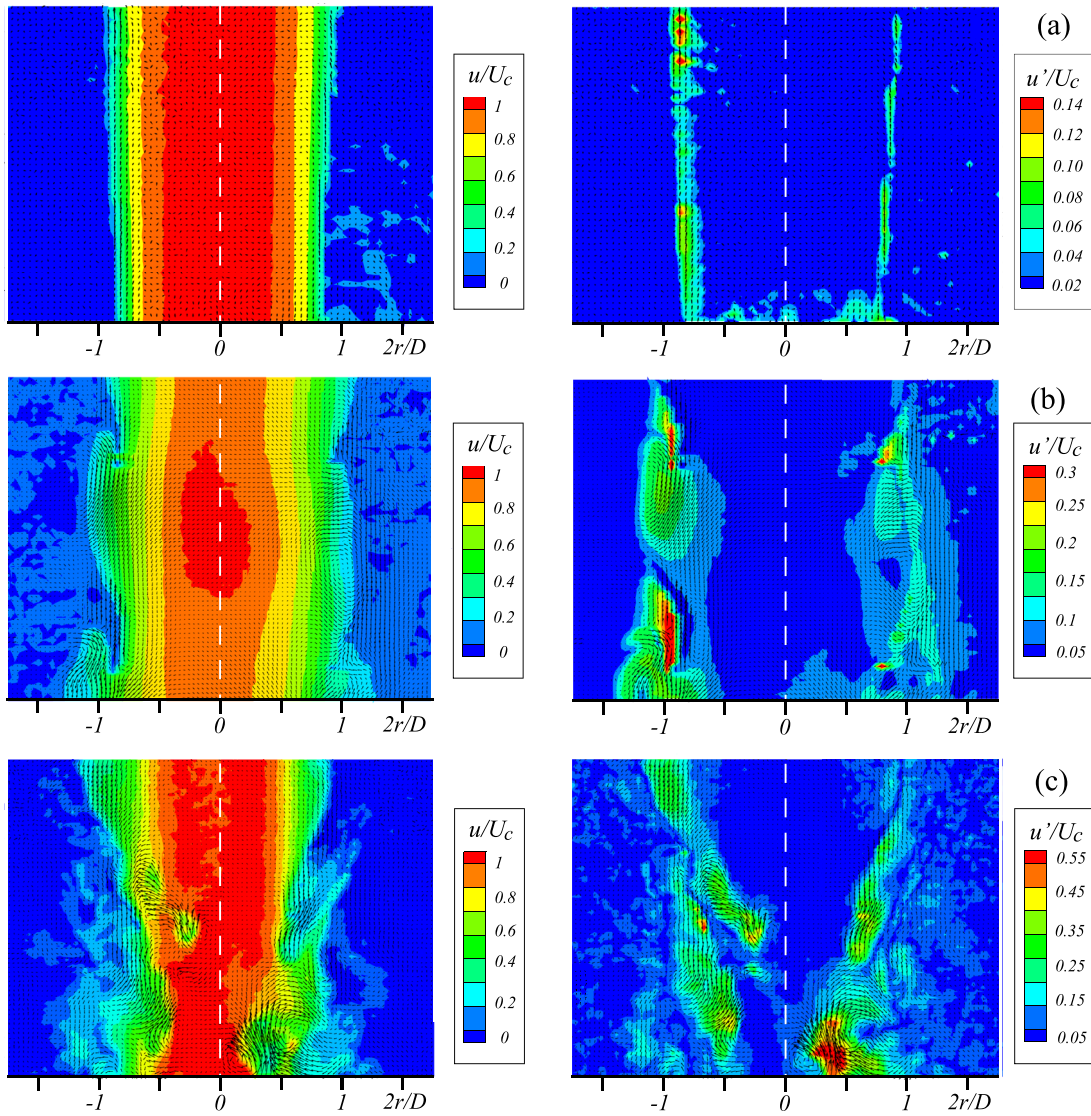


FIG. 11. Contours: Distributions of velocity magnitude (left) and velocity fluctuations (right) for the three stages of the jet evolution: laminar (a), transitional (b), and fully turbulent (c), measured by PIV. Vectors: Flow velocity fluctuation.

confirm the jet laminarity at least up to the distances shown in Fig. 14.

V. NUMERICAL MODELING OF THE FLOW IN THE DIFFUSER

To analyze the flow downstream from the first (turbulence-reducing) section of the jet-forming device, we have studied the flow in its second section. The control volume method implemented in Ansys CFX code is used. The flow is assumed to be steady and laminar; hence, Navier-Stokes equations are solved. The computational region consists of a portion of the forming device (inlet channel, diffuser, and the grid package at the diffuser outlet) and a portion of the ambient fluid.

A. Formulation of the problem

The flow in the forming device is axisymmetric, which can be simulated by considering a 3-dimensional small-angle sector with symmetry conditions assigned at the sector side

planes. This quasi-3D approach eliminates any difficulties associated with the singularity of the cylindrical coordinate system at the centerline. The computational region is a 5° , 1-element thick sector, which is split into three domains (Fig. 16): the first domain (shown in dark gray) corresponds to the flow in the tube and diffuser, the second domain (shown in light gray) corresponds to the grid package at the diffuser outlet that is simulated as porous medium, and the third domain represents the ambient fluid. The first and third domains are fluid domains, where the flow is governed by Navier-Stokes equations. The air is considered as incompressible fluid with the dynamic viscosity 1.79×10^{-5} Pa s. The second domain is an isotropic porous medium, where additional momentum source term \vec{S}_M is added to the momentum equation. The momentum loss is formulated using permeability coefficient K_{perm} and resistance loss coefficient K_{loss} as shown by the formula

$$\vec{S}_M = -\frac{\mu}{K_{perm}} \vec{U} - K_{loss} \frac{\rho}{2} |\vec{U}| \vec{U},$$

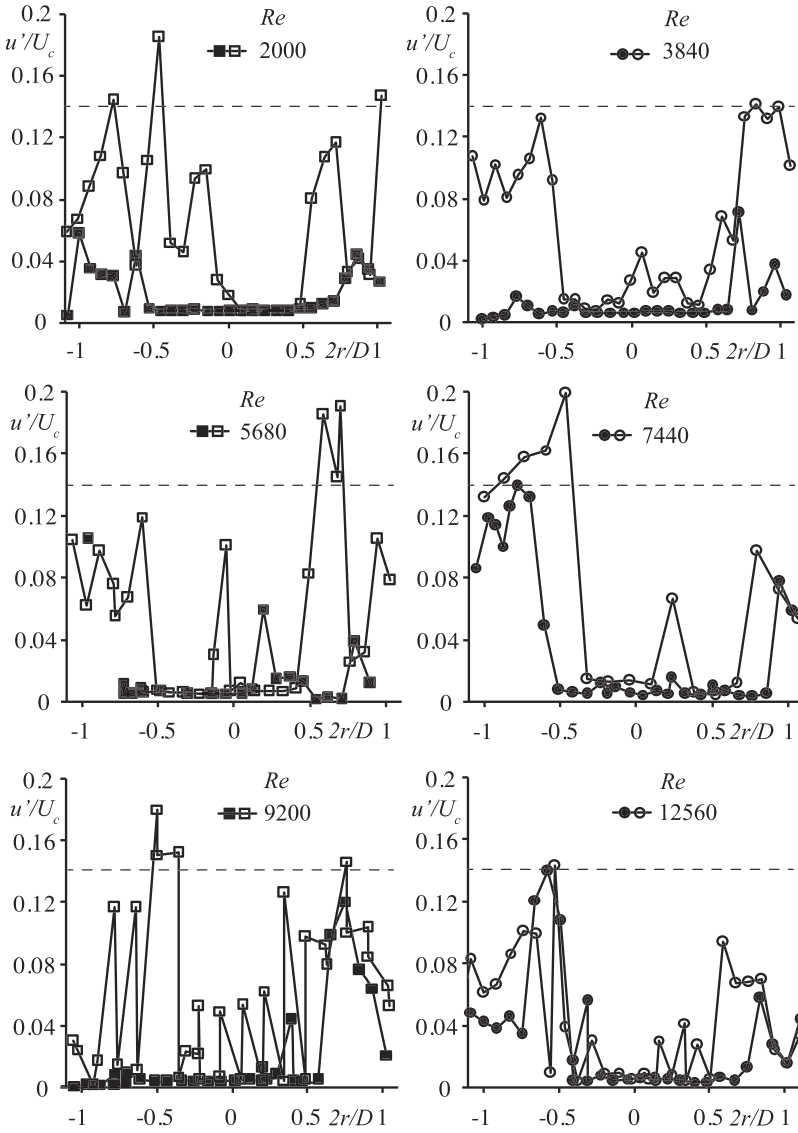


FIG. 12. Profiles of turbulent fluctuations at the distance L_{lam} and $L_{lam} + D/2$ (filled and empty marker symbols, respectively). Dashed lines show the threshold $u'/U_c = 14\%$.

where μ and ρ are the dynamic viscosity and density of the fluid, respectively, and \vec{U} is the fluid velocity. The values of permeability and resistance loss coefficients are chosen to provide the pressure drop in the porous domain equal to experimental data for the grid package obtained in a special series of experiments which is well approximated by the formula

$$\Delta p = 4.3U^2 + 35.7U, \quad (2)$$

where Δp (Pa) is the experimental pressure drop and U (m/s) is the flow velocity. Values $K_{perm} = 5 \times 10^{-11} \text{ m}^2$ and $K_{loss} = 71\,696 \text{ m}^{-1}$ for the porous domain thickness 0.1 mm are set in the model to fit the experimental pressure loss (2).

The boundary conditions (Fig. 16) are the following:

- at the inlet of the computational region, the magnitude of the normal velocity is specified;
- at the wall of the tube and the diffuser, the no-slip boundary condition $\vec{u} = 0$ is applied;
- conservative mass and momentum fluxes are assigned for both sides of interfaces between the diffuser and porous domains (interface 1) and between porous and external domains (interface 2);

- pressure equal to 10^5 Pa and zero flow direction gradient are specified at external boundaries; and
- static pressure of 10^5 Pa is specified over the outlet.

B. Numerical convergence and validation of the model

To test the numerical convergence, calculations under the same physical parameters and various mesh sizes of the calculation region have been performed. Mesh sizes are approximately 182 000 (Fig. 17) and 428 000 control volumes and the maximum of residuals in spatial iterations is 4.4×10^{-5} . The solid line (182 000) and the dashed line (428 000) in Fig. 18 demonstrate good agreement between the resulting velocity profiles downstream from the diffuser. Therefore, we conclude that the convergence in mesh size is achieved. The comparison between the velocity profiles obtained with a mesh of 428 000 volumes with maximum residuals of 4.4×10^{-5} (dashed line in Fig. 18) and 4.4×10^{-4} (gray criss-crosses in Fig. 18) shows that the profiles coincide so that the convergence in residuals is also achieved.

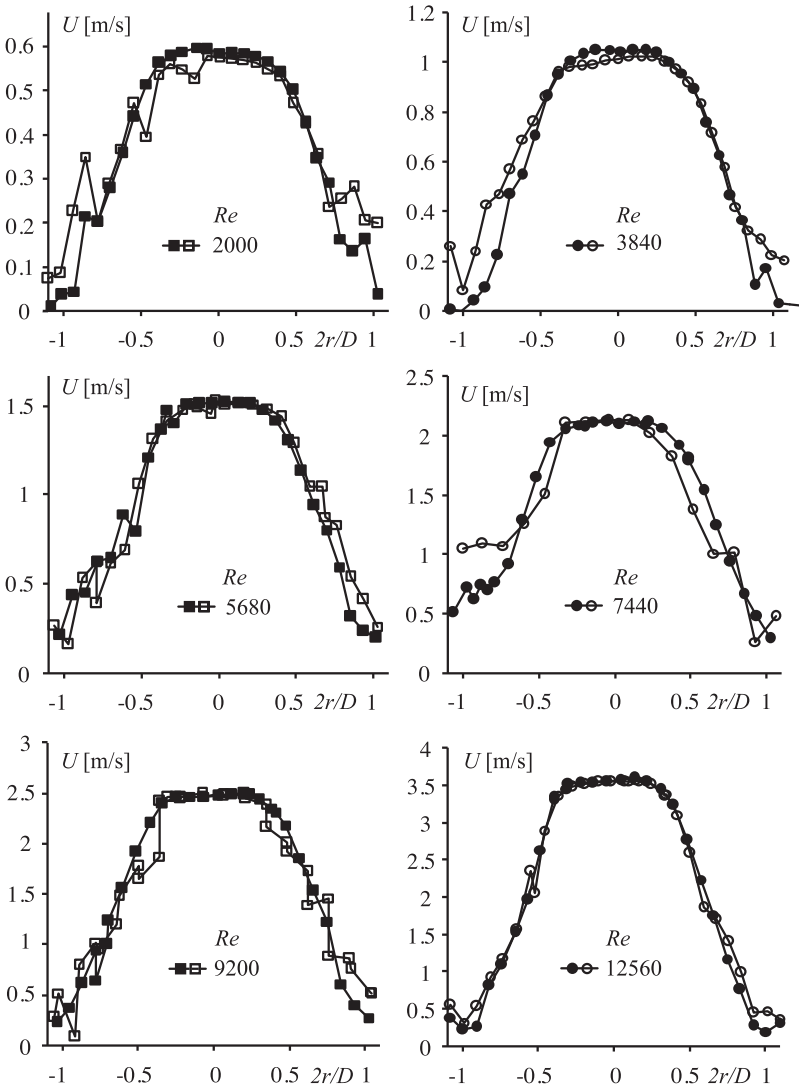


FIG. 13. Mean velocity profiles at the distance L_{lam} and $L_{lam} + D/2$ (filled and empty marker symbols, respectively).

Figure 19 shows the close agreement of calculated velocity profiles at a distance of 5 mm from the porous domain (solid lines) with experimental velocity profiles, measured at the same location (points) in a special series of tests with a higher spatial resolution of velocity measurements.

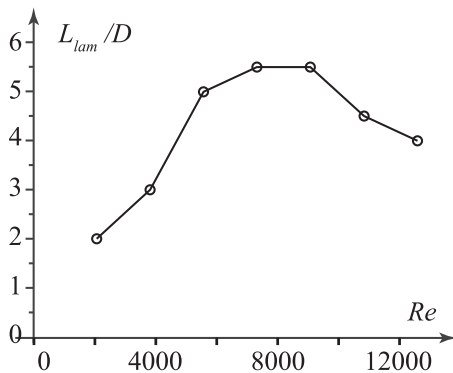


FIG. 14. Length L_{lam} of the jet laminar region versus the Reynolds number Re .

C. Results of calculations

The flow streamlines in the diffuser are shown in Fig. 20. Because of the pressure drop at the grid package (simulated as the porous medium), the flow is slowed down and radially expanded before the grid. The flow is attached to the wall for the first regime ($Re = 2000$), whereas for regimes $Re = 9200$ and $Re = 12560$, there are small local separations. The separation bubble for the regime $Re = 9200$ is shown in more detail in Fig. 21. Wall shear stress versus the longitudinal coordinate x along the tube and diffuser wall is shown in Fig. 22 for all three regimes. The dashed line in Fig. 22 confirms that the flow is attached for the first regime, while for the second and the third regimes (dashed-dotted and solid lines), the wall shear stress is negative at a small segment of the diffuser wall which corresponds to the local separation region. For higher velocity, the separation bubble is longer (its length along the x axis is 0.0195 and 0.0209 m for $Re = 9200$ and $Re = 12560$, respectively).

The appearance of the separation region inside the diffuser explains the change in the outgoing velocity profile. When the flow is attached, the velocity profile is convex in the

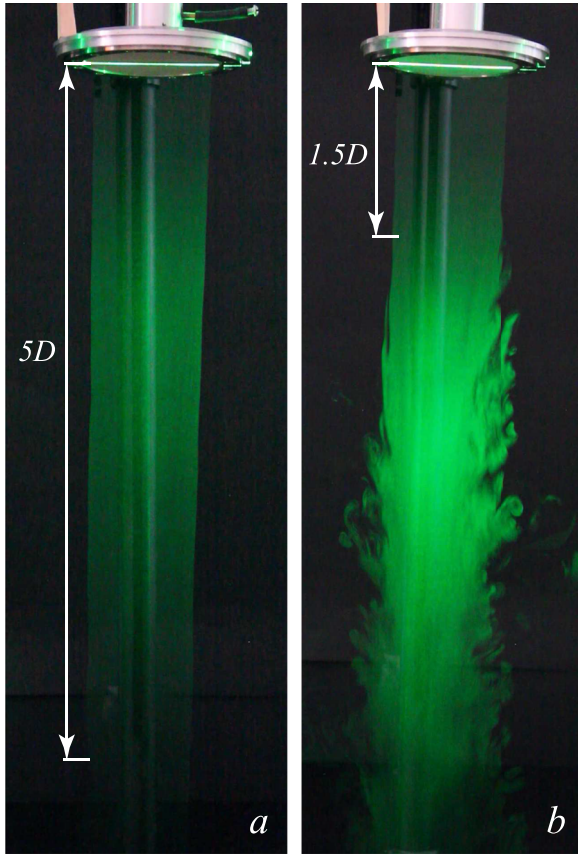


FIG. 15. Visualisation of free jets. The jet with a long laminar region at $Re = 7240$ (a) and a short laminar region at $Re = 1450$ (b).

larger part of the jet, and a single inflection point is located near the outer jet radius [Fig. 19(a)]. When the local separation occurs, the separation bubble decreases the effective cross section of the diffuser and impedes the radial flow into a thin gap between the diffuser wall and the grid package. Namely, the mass flow rate through the plane AB rated to the total flow rate (Fig. 23) is 0.534, 0.467, and 0.453 for the regimes $Re = 2000$, 9200, and 12 560, respectively. As the relative flow rate passing through the central core of the jet increases while that through the outer region decreases, this

yields the occurrence of two more inflection points in the outcoming velocity profile near $r = 0.03$ and 0.049 m [Figs. 19(b) and 19(c)]. For higher flow speed, the separation bubble is longer which results in a more pronounced dip in the velocity profile.

The steady flow analysis connects the flow structure in the diffuser with the outcoming velocity profile. Next, to establish the connection between the velocity profile and the length of the laminar region, in Sec. VI, we conduct a stability analysis of the jets.

VI. INSTABILITY PROPERTIES OF JETS

To understand the difference in laminar region lengths obtained at various regimes, we performed an analysis of the hydrodynamic stability of jets. As growing perturbations in jets are related to inviscid instability, and taking into account quite large Reynolds numbers $Re \sim 10^4$ in our experiments and almost no spreading of the jet along its laminar region, we analyzed the temporal inviscid instability within the framework of the Rayleigh equation.

Steady velocity profiles at various regimes were calculated with the numerical model described and validated in Sec. V. In the stability analysis, we neglected their development downstream from the diffuser due to large Reynolds numbers, i.e., the velocity profiles were assumed constant along the jet. After that, each profile was non-dimensionalised, taking the jet radius and maximum velocity U_c as length and velocity scales. Then in non-dimensional variables, the jet velocity $U(r)$ varies from 1 at $r = 0$ to 0 at $r = 1$ and $U(r) = 0$ for $r > 1$. To distinguish velocity profiles calculated for different regimes, we will use the Reynolds number as the profile's parameter. The resulting velocity profiles are shown in Fig. 24. In this section, the instability analysis is conducted in dimensionless form, and in Subsection VI E, the perturbation growth rates are scaled to dimensional form in the context of the laminar region length analysis.

A. Rayleigh equation and boundary conditions

After the linearisation of Euler equations around steady jet flow with a given velocity profile $U(r)$, Rayleigh³⁸ (see also

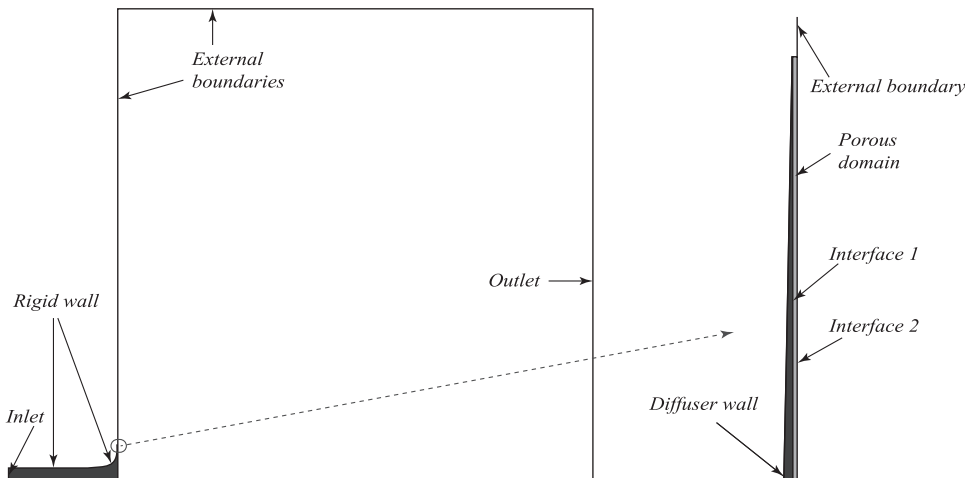


FIG. 16. Computational domain. The bottom line shows the axis of the forming device.

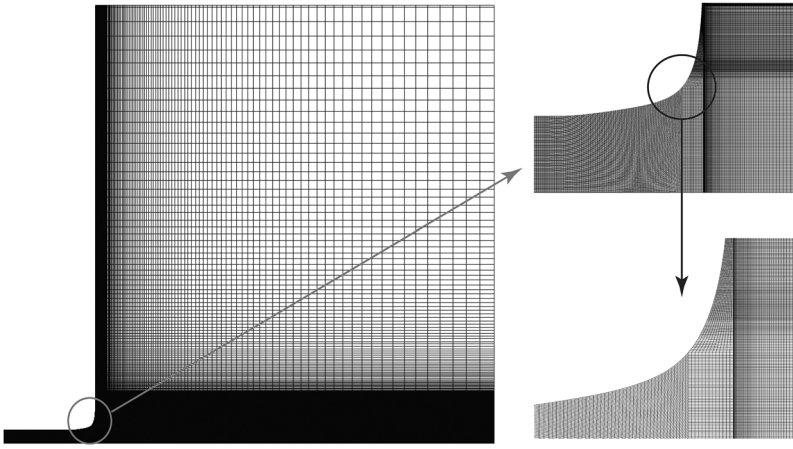


FIG. 17. Computational mesh.

the work of Batchelor and Gill⁴) obtained a single equation for the radial velocity perturbation for round jets in a cylindrical coordinate system,

$$(U(r) - c) \frac{d}{dr} \left(\frac{r}{n^2 + \alpha^2 r^2} \frac{d(rG(r))}{dr} \right) - (U(r) - c) G(r) - rG(r) \frac{d}{dr} \left(\frac{rU'(r)}{n^2 + \alpha^2 r^2} \right) = 0, \quad (3)$$

where $G(r)$ is the amplitude of the radial velocity fluctuation,

$$u_r = iG(r)e^{i(\alpha x + n\varphi - \omega t)},$$

$\alpha \in \mathbb{R}$ and $n \in \mathbb{Z}$ are axial and azimuthal wave numbers, ω is the frequency, and $c = \omega/\alpha$ is the phase speed.

Perturbation $G(r)$ should satisfy two boundary conditions. First, at $r = \infty$, the radiation condition must be satisfied. We will assume that for $r > 1$, the fluid is at rest; that is, $U(r) = 0$. With zero steady velocity, (3) has two linearly independent solutions, $I'_n(\alpha r)$ and $K'_n(\alpha r)$, which are the derivatives with respect to r of modified Bessel functions of the first and second kinds. As only K'_n satisfies the radiation condition, we have

$$G(r) = C \frac{dK_n(\alpha r)}{dr}, \quad r \geq 1. \quad (4)$$

Then we may transfer the radiation condition from infinity to $r = 1$ by matching (4) with the solution at $r < 1$ by putting

$$\frac{G'(r)}{G(r)} = \frac{K''_n(\alpha r)}{K'_n(\alpha r)}, \quad r = 1. \quad (5)$$

The second boundary condition at $r = 0$ is not as obvious and was discussed in detail by Batchelor and Gill.⁴ It can be summarised as

$$\begin{aligned} G(0) &= 0, & n &= 0, \\ G'(0) &= 0, & n &= 1, \\ G(r) &\sim r^{n-1}, & r \rightarrow 0, & n > 1. \end{aligned} \quad (6)$$

For each $\alpha \in \mathbb{R}$, $n \in \mathbb{Z}$ the boundary-value problem for the Rayleigh equation (3), (5), and (6) defines an eigenvalue problem to find $c(\alpha, n) \in \mathbb{C}$.

B. Numerical method

The eigenvalue problem (3), (5), and (6) was solved numerically. The boundary-value problem was first reduced to an initial-value problem with initial conditions specified at $r = \varepsilon = 10^{-5}$ (to avoid numerical singularity of the coordinate system at $r = 0$),

$$\begin{aligned} G(\varepsilon) &= \varepsilon, & G'(\varepsilon) &= 1, & n &= 0, \\ G(\varepsilon) &= 1, & G'(\varepsilon) &= \varepsilon, & n &= 1, \\ G(\varepsilon) &= C\varepsilon^{n-1}, & G'(\varepsilon) &= C(n-1)\varepsilon^{n-2}, & n &> 1, \end{aligned} \quad (7)$$

where a constant C was selected to obtain the eigenmode amplitude of the order of 1. With these initial conditions, the Rayleigh equation was solved by the Runge-Kutta method and the value

$$F(\alpha, n, c) = G'(1)K'_n(\alpha) - G(1)K''_n(\alpha)$$

was calculated. Based on the convergence study, $N = 300$ points per segment $[0; 1]$ were used in the Runge-Kutta method. For each α and n , the root $c(\alpha, n)$ of the equation

$$F(\alpha, n, c) = 0 \quad (8)$$

was found by the secant method (with recalculation of the Rayleigh equation solution at each iteration).

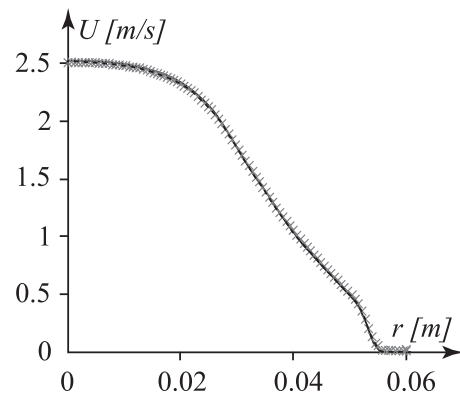


FIG. 18. Convergence in mesh size and in maximum residual. Velocity profiles for mesh sizes 182 000 volumes and maximum residual 4.4×10^{-5} (solid line), 428 000 volumes and maximum residual 4.4×10^{-5} (dashed line), and 428 000 volumes and maximum residual 4.4×10^{-4} (gray criss-crosses).

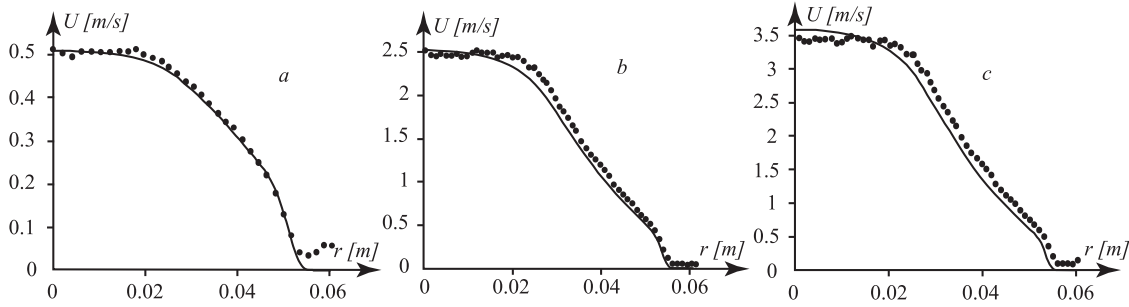


FIG. 19. Comparison of experimental (points) and calculated (solid lines) jet velocity profiles at a distance of 5 mm from the diffuser outlet for the regimes $Re = 2000$ (a), 9200 (b), and $12\,560$ (c).

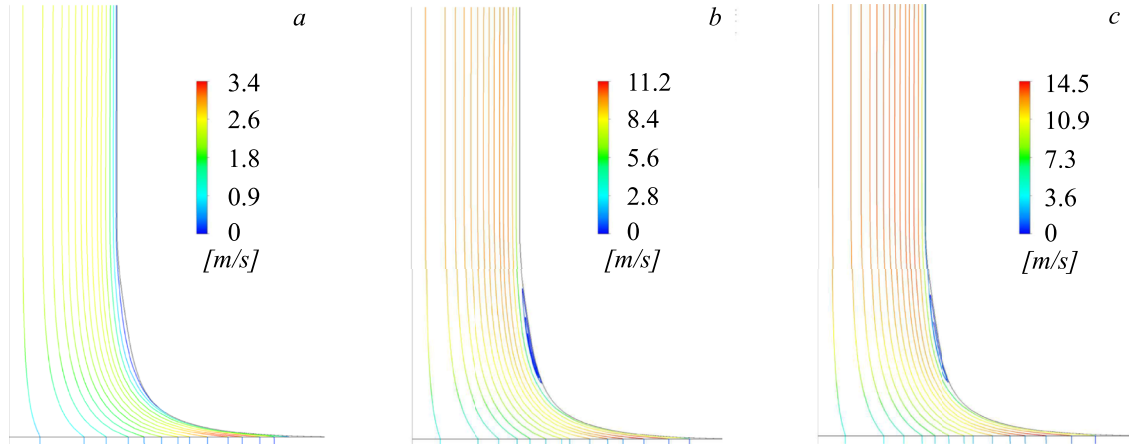


FIG. 20. Streamlines in the diffuser for the regimes $Re = 2000$ (a), 9200 (b), and $12\,560$ (c).

For every n , calculations of $c(\alpha)$ have been conducted independently. First, the neutral mode (α_s, c_s) was found. Its eigenvalue is $c_s = U(r_s)$, where r_s is a root of the equation^{4,38}

$$Q'(r) = 0, \quad Q(r) = \frac{rU'}{n^2 + \alpha^2 r^2}. \quad (9)$$

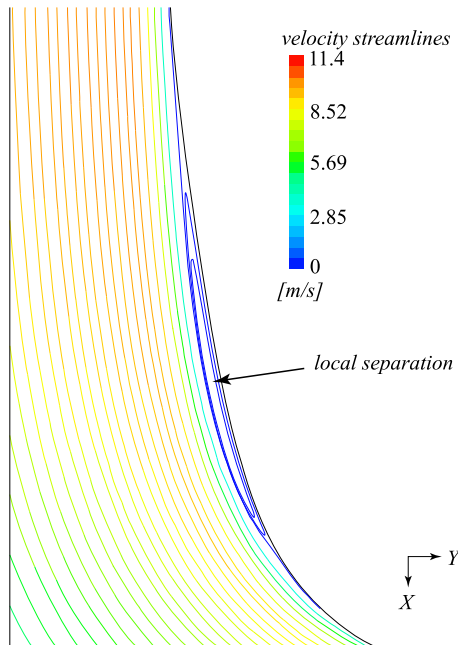


FIG. 21. Local separation in the diffuser for $Re = 9200$.

Since this equation is a generalisation of an inflection-point condition $U''(r) = 0$ for planar flows to axisymmetric flows, we will call its roots r_s generalised inflection points. For each branch of real roots $c_s(\alpha)$ of (9), $\alpha = \alpha_s$ was found to satisfy (8). If such α_s exists, that is, a neutral mode is found, then the point c_s is the origin of the curve $c(\alpha)$ in the complex c -plane lying in a Howard semicircle,^{11,16} which gives a branch of growing perturbations. By the step-by-step change of α , starting from

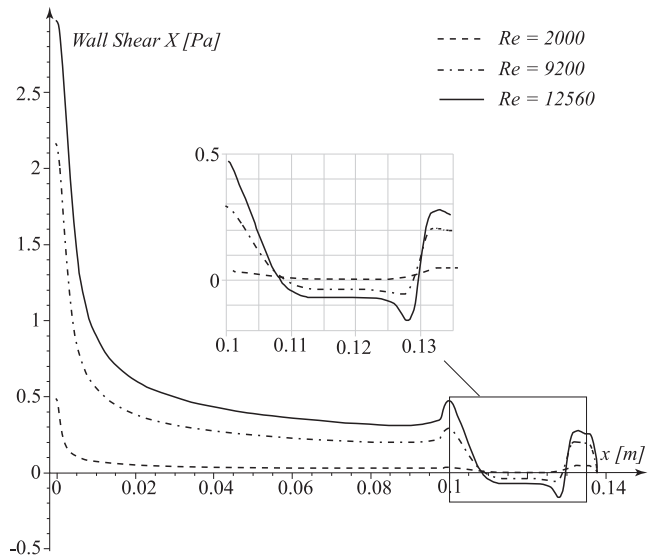


FIG. 22. Wall shear stress (x -component) versus the coordinate x along the jet axis for $Re = 2000$ (dashed line), 9200 (dashed-dotted line), and $12\,560$ (solid line).

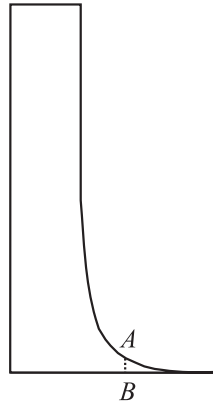


FIG. 23. Line AB for the calculation of relative mass flow.

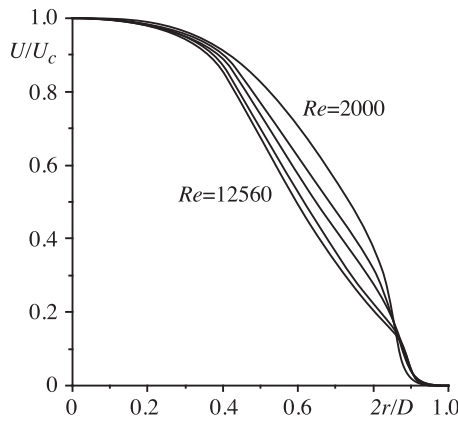


FIG. 24. Dimensionless steady velocity profiles $U(r)$ obtained for $Re = 2000, 3840, 5680, 9200, 12560$.

α_s , eigenvalues $c(\alpha)$, $\text{Im } c > 0$, were calculated until either the eigenvalue again becomes real or $\alpha = 0$.

The most simple case of finding neutral perturbations is $n = 0$ because Eq. (9) is reduced to

$$(U'/r)' = 0, \tag{10}$$

and locations of generalised inflection points do not depend on α and are governed only by the velocity profile. Figure 25 shows its roots versus Re . For $2000 \leq Re \leq 12560$, there are three roots; that is, three neutral perturbations exist. The first, denoted “s1,” is governed by the generalised inflection point

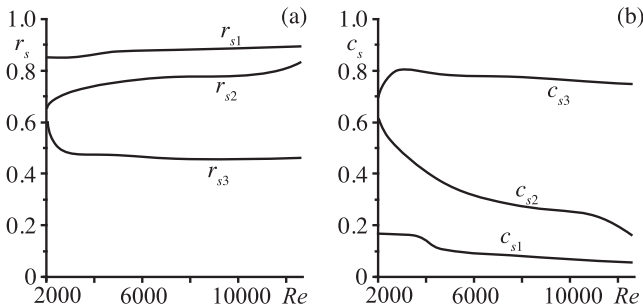


FIG. 25. Generalised inflection points r_s [roots of (10)] (a) and phase speed of neutral perturbations $c_s = U(r_s)$ (b) versus Re for $n = 0$.

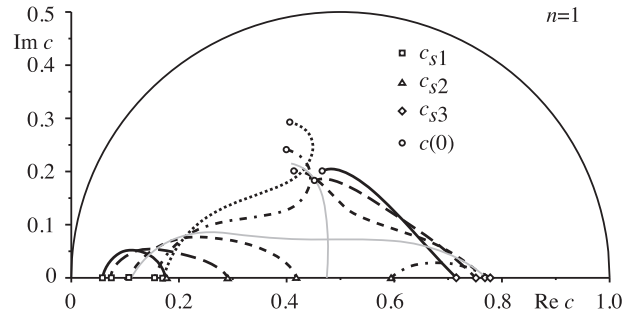
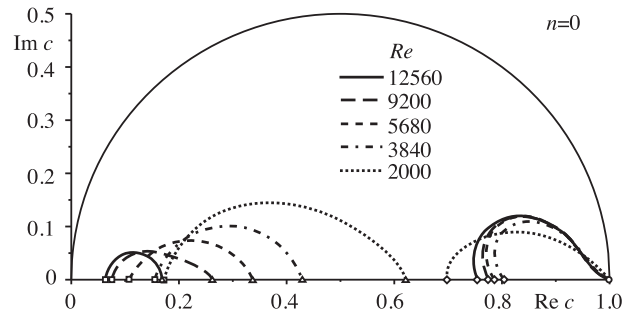


FIG. 26. Branches $c(\alpha)$ of growing perturbations and a Howard semicircle in the complex c -plane for $n = 0, 1$. Results for $Re = 12560$ (solid line), 9200 (long dashed line), 5680 (short dashed line), 3840 (dashed-dotted line), 2000 (dotted). For $n = 1$, the thin gray line represents the results for $Re = Re_{saddle}$.

of velocity profiles which is the closest to the outer jet radius. Two other roots, denoted “s2” and “s3,” are located closer to the jet centre, and for Re slightly below 2000, they collapse and disappear.

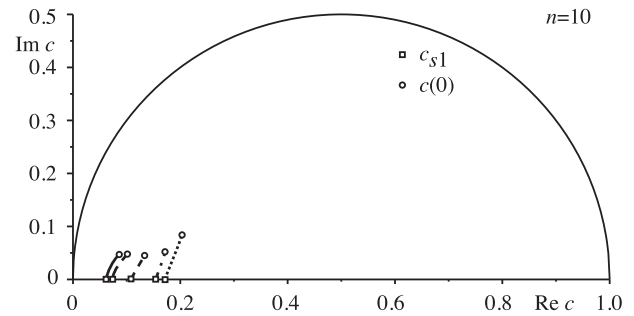
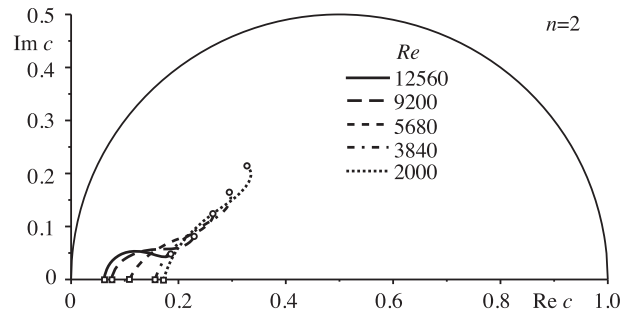


FIG. 27. Branches $c(\alpha)$ of growing perturbations and a Howard semicircle in the complex c -plane for $n = 2, 10$. Results for $Re = 12560$ (solid line), 9200 (long dashed line), 5680 (short dashed line), 3840 (dashed-dotted line), 2000 (dotted).

To obtain solutions that are limit of viscous solutions at vanishing viscosity, Lin's rule^{11,28} must be enforced; that is, an integration of the Rayleigh equation must be conducted above the critical point r_c (for $U' < 0$). For growing perturbations, $\text{Im } c > 0$, the critical point lies in the bottom half-plane, $\text{Im } r_c < 0$, which means that the integration along the real segment $[0; 1]$ is in accordance with Lin's rule. Damped perturbations need integration in the complex r -plane along a contour passing above the critical point; however, such perturbations do not affect the jet stability and are not considered in this study.

To check the validity of the computational code, a family of 'top-hat' profiles representing a smoothed axisymmetric vortex sheet was studied first. For the decreasing length of the segment, where the flow speed reduces from the core speed to zero, calculated eigenvalues $c(\alpha)$ tend to the closed-form solution of the eigenvalue problem for the vortex sheet.⁴ Hence, the code is validated and can be used for stability calculations.

C. Results

We will start the observation of results with the velocity profile at $Re = 12\,560$. For $n = 0$ and 1, there exist three neutral modes $c = c_s$ and two branches of growing perturbations $c(\alpha)$, as shown in Fig. 26. One branch connects two neutral eigenvalues c_{s1} and c_{s2} corresponding to two generalised inflection points farthest from the centre; the segment of wavenumbers $[\alpha_{s1}; \alpha_{s2}]$ corresponds to this branch. The other branch connects the neutral eigenvalue c_{s3} corresponding to the generalised inflection point closest to the jet centre, with $c = 1$ ($n = 0$) or $c = 0.468 + 0.203i$ ($n = 1$); the latter values are reached at $\alpha = 0$ so that the range of wavenumbers corresponding to this branch is $[0; \alpha_{s3}]$. For $2 \leq n \leq n_{\max} = 74$, only one branch $c(\alpha)$ exists for $\alpha \in [0; \alpha_{s1}]$ which ends at a point $c(0)$ in the upper half-plane (Fig. 27). For $n > n_{\max}$, no neutral or growing eigenmodes exist. Figure 28 shows dimensionless growth rates $\text{Im } \omega(\alpha)$. As shown, the maximum growth rate $\max_{\alpha} \text{Im } \omega = 0.734$ is reached at the first

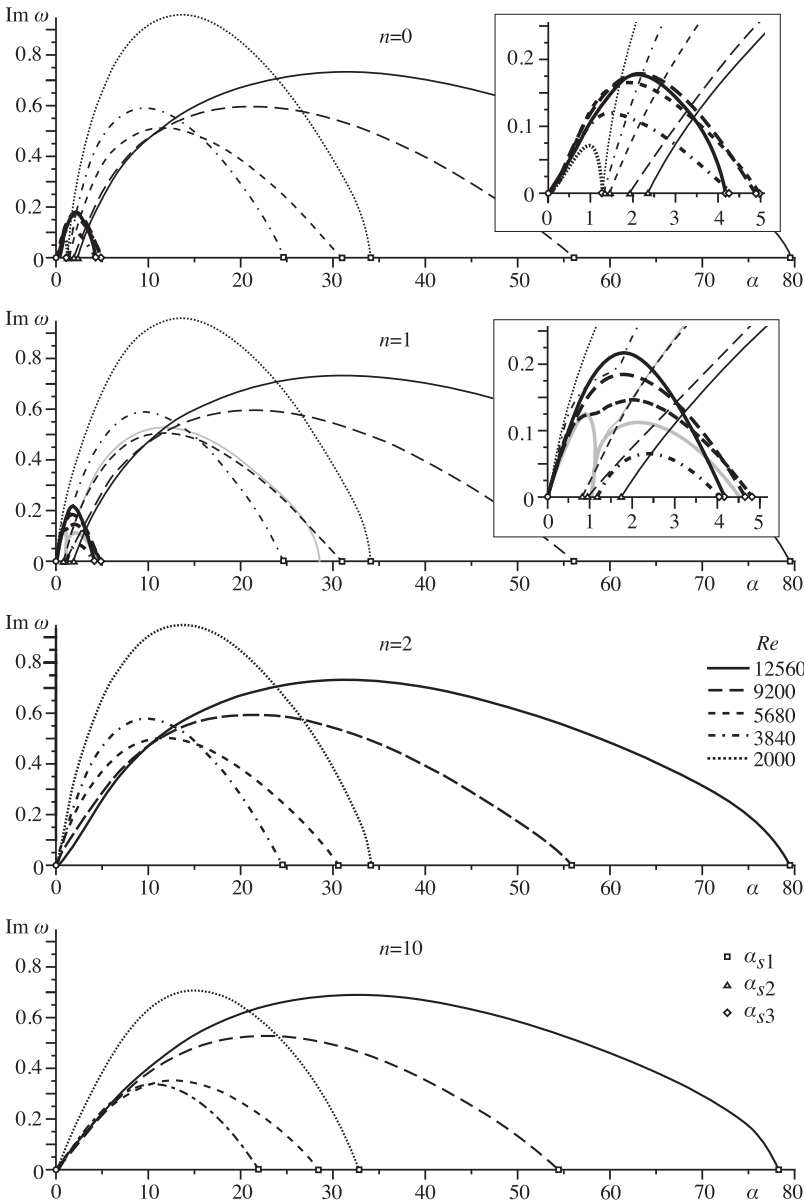


FIG. 28. Growth rates of growing perturbations $\text{Im } \omega(\alpha)$ for $n = 0, 1, 2, 10$. Results for $Re = 12\,560$ (solid line), 9200 (long dashed line), 5680 (short dashed line), 3840 (dashed-dotted line), 2000 (dotted). For $n = 1$, the gray lines represent the results for $Re = Re_{\text{saddle}}$.

TABLE II. Maximum dimensionless growth rates $\max_{\alpha} \text{Im } \omega$ for different velocity profiles.

Re	$n=0$	$n=1$	$n=2$	$n=10$	$n=20$
2000	0.961	0.958	0.949	0.710	0.295
3840	0.591	0.588	0.578	0.335	0.027
5680	0.509	0.507	0.501	0.352	0.110
9200	0.598	0.597	0.593	0.529	0.380
12560	0.734	0.733	0.732	0.691	0.570

branch and is mostly governed by the point r_{s1} . For increasing n , the maximum growth rate slowly decreases to 0, as shown in Table II.

A similar behaviour is observed for other profiles. In all cases, for $2 \leq n \leq n_{\max}$, only one branch of growing perturbations associated with generalised inflection point r_{s1} exists (Figs. 27 and 28), and no growing perturbation exists for $n > n_{\max}$. The value of n_{\max} varies: $n_{\max} = 50, 27, 22, 31$ for $Re = 9200, 5680, 3840, 2000$, respectively.

For $n=1$, an interesting phenomenon of the saddle point of $c(\alpha)$ is found at $Re = Re_{\text{saddle}} = 4892$ (Fig. 26). While for $Re > Re_{\text{saddle}}$, the branch linking the two neutral perturbations connects c_{s1} and c_{s2} , for $Re < Re_{\text{saddle}}$, it switches to connecting c_{s2} and c_{s3} . At a decreasing Re , the values of c_{s2} and c_{s3} become closer to each other and collapse at $Re = 2932$. At a lower Re , this branch of perturbations becomes damped for all α .

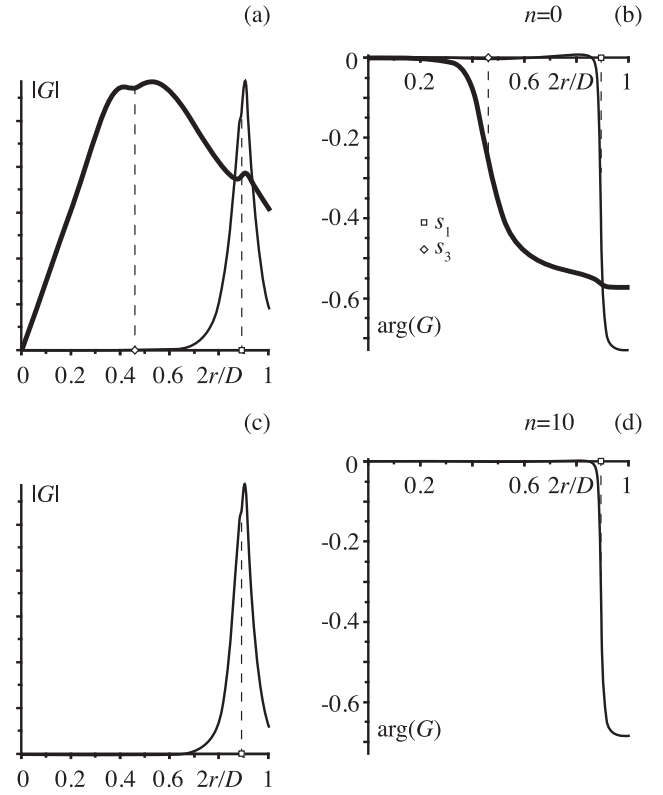
For $n=0$, no such collapse occurs at $2000 \leq Re \leq 12560$, and the branches $c(\alpha)$ do not change their topology.

Figure 29 shows the examples of eigenmodes corresponding to the maximum growth rate at $Re = 9200$. For $n=0$ and the branch connecting c_{s1} and c_{s2} (shown by thin curves), the maximum growth rate is achieved at $\alpha \approx 21.2$. This mode is concentrated around the point r_{s1} , where the maximum amplitude is located and significant phase change occurs. For the branch connecting c_{s3} and $c=1$ (shown by bold curves), the fastest growing eigenmode corresponds to $\alpha \approx 2.1$. The maximum amplitude and the most of the phase change occur in the internal region of the jet, near the point r_{s3} . Note that according to Fig. 28, the maximum growth rate of the first branch is essentially larger than of the second; hence, it is natural to expect that the first branch triggers the transition to turbulence. For $n=10$, only the first branch of eigenmodes exists. Maximum growth rate corresponds to $\alpha \approx 22.6$, and the amplitude and phase distributions are similar to those at $n=0$.

Table II shows dimensionless maximum growth rates. In all profiles considered, the most rapidly growing perturbation is the axisymmetric mode ($n=0$); however, growth rates for helical perturbation with small n are very close to those at $n=0$. It is seen that among various velocity profiles, the growth rate reaches a maximum at $Re = 2000$, decreases as the Re increases until $Re = 5680$, and then increases.

D. Experimental validation of theoretical results

Several earlier studies (e.g., by Cohen and Wygnanski⁷) have clearly shown that the initial growth of perturbations in jets follows the inviscid linear instability theory and the distance to the transition depends on corresponding linear

FIG. 29. Amplitude [(a) and (c)] and phase [(b) and (d)] of the fastest growing eigenmodes for $n=0$ [(a) and (b)] and $n=10$ [(c) and (d)] at $Re = 9200$.

growth rates. However, to validate our instability calculations, we performed a limited amount of additional measurements of jet fluctuations in the transition region. For the regime $Re = 3840$, we measured samples of velocity fluctuations at the distances $2D$ and $4D$ downstream from the orifice. For each sample, 3 s in length, the spectrum of velocity fluctuations was calculated in several points. Figures 30(a) and 30(b)

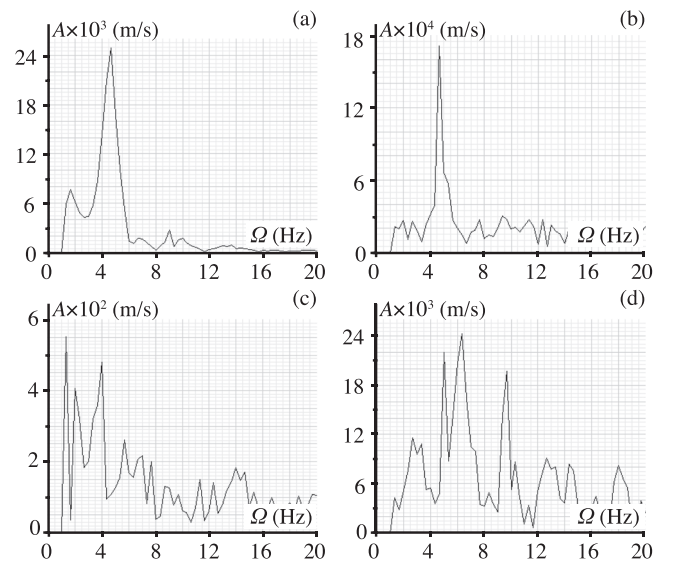
FIG. 30. Spectra of the flow velocity fluctuations at the distance $L = 2D$ [(a) and (b)] and $4D$ [(c) and (d)] from the orifice. The probe is located near the outer jet radius [(a) and (c)] and near the jet centre [(b) and (d)]. Regime $Re = 3840$.

TABLE III. Dimensional physical frequencies $\Omega = \omega \times (2U_c/D)/(2\pi)$ (Hz) of the fastest growing perturbations.

Re	Ω_1	Ω_{\max}	Ω_2
2 000	2.31	3.58	5.44
3 840	3.25	4.99	7.00
5 680	4.40	6.54	8.92
9 200	10.48	12.53	14.50
12 560	10.27	18.71	28.81

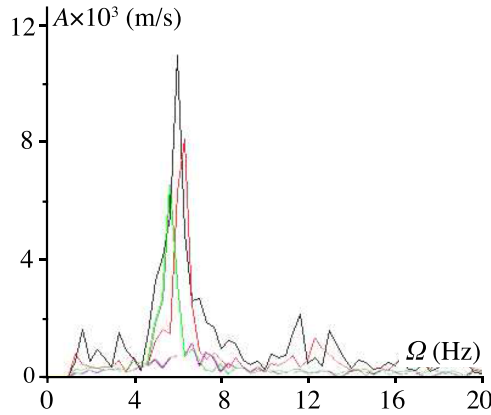


FIG. 31. Spectra of the flow velocity fluctuations at the distance $L = 4.5D$ from the orifice. Various probe locations inside the jet core are shown by colours. Regime $Re = 5680$.

show the results for a point near the jet boundary (where the generalised inflection point $s1$ is located) and in the central core for the axial distance $2D$, where the flow is laminar. In all spatial locations, the dominant frequency is 4.6 Hz.

To compare these results with the instability calculations, we calculated the frequency ω_{\max} corresponding to the fastest growing wave (Fig. 28) and the frequency range $\omega_1 < \omega < \omega_2$ of perturbations with $\text{Im } \omega \geq 0.8 \max \text{Im } \omega$, that is, those growing not slower than 80% of the fastest growing wave. The results are shown in Table III in dimensional form. As shown, the experimental dominant frequency is quite close to the theoretical frequency of the most growing perturbation Ω_{\max} (8% error) and is certainly in the range $\Omega_1 < \Omega < \Omega_2$.

Figures 30(c) and 30(d) show spectra of velocity fluctuations in the same spatial locations of the jet cross section but farther downstream from the orifice, namely, at the distance $4D$. It is seen that the transition to turbulence has already started; fluctuations near the outer jet radius do not have any dominant frequency. On the other hand, in the jet centre, where the amplitude of fluctuations is substantially lower, a frequency of 4.9 Hz that is close to dominant at the distance $2D$ is present. However, the growth of other frequencies is also clearly seen which signifies that the nonlinear transformation of the perturbation has started in the jet centre as well.

To verify the trend of the frequency increase of the fastest growing perturbation with the flow speed increase, measurements at $Re = 5680$ are also conducted. Figure 31 shows that the dominant frequency of velocity fluctuations in the jet core is 6.0 ± 0.5 Hz which is in accordance with theoretical data shown in Table III.

To measure the convective speed of perturbations, the flow in the transition region was visualised through particle image velocimetry at the regime $Re = 2759$. Figure 32 shows snapshots of the axial velocity and vorticity distributions by contours and velocity perturbations by vectors at the distance $L/D \approx 3.5$ from the orifice. Coherent structures in the flow are clearly seen. Their convective speed is $c_{\text{exp}} = 0.189$ m/s which is in reasonable agreement with the calculated phase speed of the fastest growing wave $c_{\text{calc}} = 0.156$ m/s, given that the coherent structures in Fig. 32 are in their nonlinear stage of evolution, and the phase speed, as well as wave length and frequency, can change compared with the linear stage. On the other hand, calculated growth rate $\text{Im } \omega$ of the wave having the phase speed c_{exp} is equal to $0.8 \max \text{Im } \omega$; that is, the theory also predicts its significant growth.

In Figs. 30 and 32, the maximum amplitude of the flow fluctuation is located near the outer jet boundary, where the generalised inflection point $s1$ is located. The linear theory (Fig. 29) shows that eigenmodes corresponding to the fastest growing perturbations also have a sharp peak near $s1$; that is, not only the frequency and convective speed but also the observed spatial structure of the jet fluctuations are in agreement with the theory.

Thus, we conclude that the transition to turbulence is triggered by the fastest linearly growing perturbations which

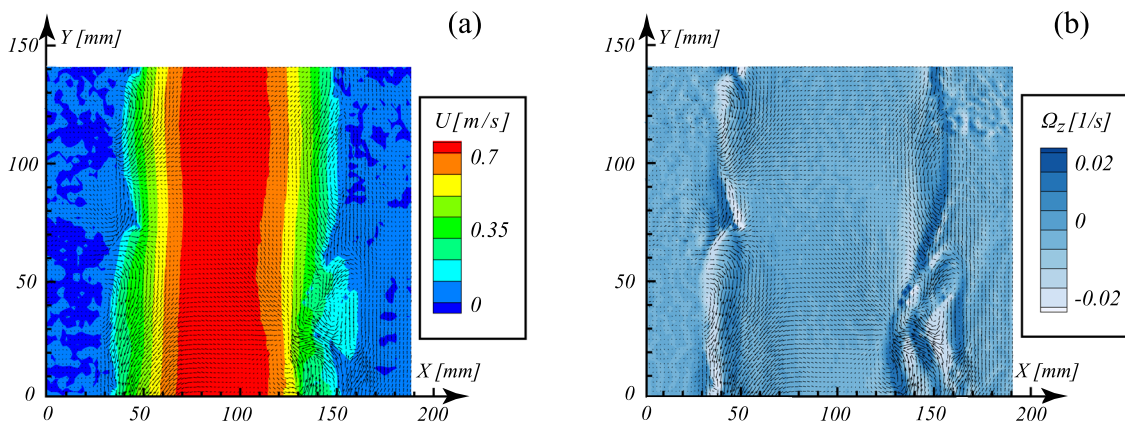


FIG. 32. Flow visualisation in the transition region by PIV. Contours: Axial velocity (a) and vorticity (b). Vectors: Flow velocity fluctuation. Regime $Re = 2759$.

TABLE IV. Maximum dimensional growth rates $\max_{\alpha} \text{Im } \omega \times (2U_c/D)$ (Hz) for different velocity profiles.

Re	$n = 0$	$n = 1$	$n = 2$	$n = 10$	$n = 20$
2 000	8.008	7.983	7.908	5.917	2.458
3 840	9.850	9.800	9.633	5.583	0.450
5 680	12.725	12.675	12.525	8.800	2.750
9 200	24.917	24.875	24.708	22.042	15.833
12 560	42.817	42.758	42.700	40.308	33.250

validates the use of linear instability analysis for the estimate of the distance to transition.

E. Length of laminar portion of the jet

To explain the observed length of the laminar portion of the jet, consider growth rates of the fastest growing wave at different regimes. In dimensionless form, the maximum growth rate is reached at $Re = 2000$ (Table II). However, when scaled back to dimensional values (Table IV), the maximum growth rate monotonically increases when Re increases.

Based on these results, we can now explain the existence of the optimal regime corresponding to the maximal length of the laminar region of the jet (Fig. 14). The transition to turbulence occurs because of growing perturbations, whose amplitude depends on, first, initial amplitudes and, second, growth rates. For small Re , we have relatively high levels of incoming turbulence (Fig. 9), and initial amplitudes of perturbations are therefore large which yields turbulisation at a relatively short distance. When the flow speed increases, the turbulence level drops (Fig. 9), and the laminar region length increases. However, at larger Re , growth rates become larger and larger so that despite low initial amplitudes, the perturbations significantly grow closer to the diffuser which again yields a shorter laminar region. By improving the balance between initial amplitudes and growth rates, it is possible to further improve the optimal regime and increase the laminar region length even more than obtained in this study.

VII. CONCLUSIONS

In this paper, we have demonstrated the formation of laminar jets with a diameter of $D = 0.12$ m at Reynolds

numbers $\sim 10\,000$ with a novel compact device of the size $\sim 1.5D$. Experimental results confirm the laminarity of the flow up to the distance of $5.5D$ downstream from the forming unit for the optimal velocity regime which is not accessible for other known methods of laminar jet formation.

To explain the existence of the optimal regime which corresponds to the longest laminar region, a steady flow analysis in the forming unit has been conducted. The correlation between the flow structure and outgoing velocity profile has been established, and the appearance of two additional inflection points in the jet profile at high-speed regimes is explained by the appearance of the local laminar separation bubble inside of the diffuser. To connect the velocity profile with the length of the laminar region, an inviscid stability analysis of the jet has been conducted and verified by experiments. It is shown that the laminar region length depends on the balance between the initial turbulence level and the growth rates of perturbations. In the experiments, for less-than-optimal flow velocities, the turbulence level increased, while for higher velocities, the perturbation growth rates increased, which both resulted in shorter laminar regions. Improving this balance, either by further decreasing the incoming turbulence level or by changing growth rates through modifying the velocity profile (by changing the diffuser wall shape and grid properties), gives the potential to obtain longer laminar jets with the same design of the jet-forming unit.

Figure 33 shows the comparison of the laminar jet lengths obtained by different authors and in this study. As shown, there are no previously available results for $Re > 6700$; that is, the transition at large Re in other studies occurred almost immediately. The dashed curve shows the envelope of results of other authors, given by the expression

$$L_{lam}/D = 1.3 \times 10^7 Re^{-1.6}.$$

It is clearly seen that laminar jets obtained in this study perfectly lie within this envelope, but correspond to essentially larger Reynolds numbers that were achieved previously.

More important is that all the “best” results for $Re \leq 6700$ available in the literature so far^{21,23,26,41} are obtained by the “pipe” method and use a very small orifice diameter $D \sim 1$ mm or less, with the exception of those of Kozlov *et al.*,²³ who used the pipe of $D = 20$ mm. Generally, the organisation of the pipe flow can be improved to obtain a

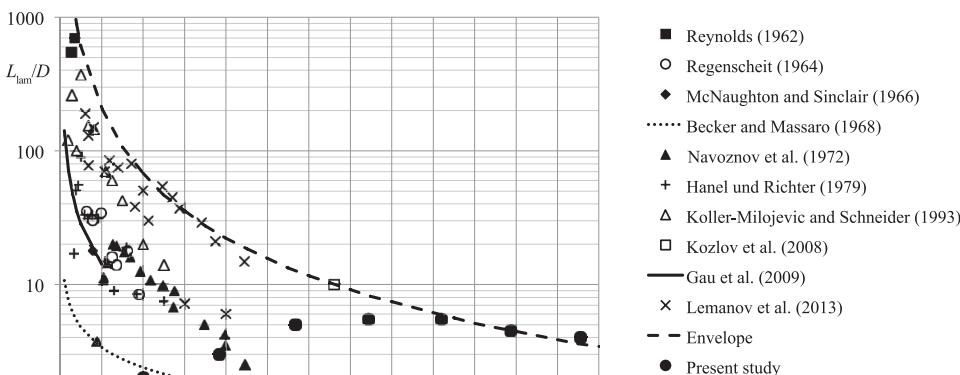


FIG. 33. Comparison of the lengths of the jet laminar portion obtained by different authors^{5,13,15,21,23,26,31,36,39,41} and in the present study. The Reynolds number is based on the orifice diameter and average velocity.

Poiseuille flow at larger Re ; however, as argued in Sec. I B, this method cannot be scaled to wider jets in real applications, as the pipe length would be huge. In particular, it is almost impossible to create a laminar jet of $D = 120$ mm, similar to the one investigated in this study, with the use of the pipe flow.

Further development of the proposed method of laminar jets formation is important for both fundamental and applied studies. From a fundamental point of view, a laminar jet of such a large diameter and length can be used for experimental investigations of perturbation growth and the development of turbulence in free jets of various velocity profiles in “natural” conditions and with external excitation. To this day, very limited data are available on this matter, primarily because of the impossibility of creating laminar jets with large diameters (~ 0.1 m) and sufficient lengths and the difficulties of carefully measuring small-scale jets.

With respect to possible applications, the technology presented in this paper can be used to create air curtains for the protection of objects in various technological processes and medicine through the formation of laminar jets of clean air or other gases which are not mixed with the ambient medium.

ACKNOWLEDGMENTS

We thank E. Zayko for her help in writing the computational code for the stability analysis. The work is supported by Russian Foundation for Basic Research Grant No. 18-38-00745.

- ¹Abramovich, G. N., *Theory of Turbulent Jets* (Nauka, 1960) (in Russian).
- ²Alekseenko, S. V., Dulin, V. M., Kozorezov, Y. S., Markovich, D. M., Shtork, S. I., and Tokarev, M. P., “Investigation of stability of subsonic gas microjet,” *Flow, Turbul. Combust.* **87**, 569–595 (2011).
- ³Arakeri, J. H., Das, D., and Srinivasan, J., “Bifurcation in a buoyant horizontal laminar jet,” *J. Fluid Mech.* **412**, 61–73 (2000).
- ⁴Batchelor, G. K. and Gill, A. E., “Analysis of the stability of axisymmetric jets,” *J. Fluid Mech.* **14**(4), 529–551 (1962).
- ⁵Becker, H. and Massaro, T. A., “Vortex evolution in a round jet,” *J. Fluid Mech.* **31**, 435 (1968).
- ⁶Chernyavsky, B., Wu, T. C., Péneau, F., Bénard, P., Oshkai, P., and Djilali, N., “Numerical and experimental investigation of buoyant gas release: Application to hydrogen jets,” *Int. J. Hydrogen Energy* **36**(3), 2645–2655 (2011).
- ⁷Cohen, J. and Wygnanski, I., “The evolution of instabilities in the axisymmetric jet. Part 1. The linear growth of disturbances near the nozzle,” *J. Fluid Mech.* **176**, 191–219 (1987).
- ⁸Crow, S. C. and Champagne, F. H., “Orderly structure in jet turbulence,” *J. Fluid Mech.* **48**(3), 547–591 (1971).
- ⁹DeBonis, J. R. and Scott, J. N., “Large-eddy simulation of a turbulent compressible round jet,” *AIAA J.* **40**(7), 1346–1354 (2002).
- ¹⁰Deich, M. E., *Technological Gas Dynamics* (Gosenergoizdat, 1961) (in Russian).
- ¹¹Drazin, P. G. and Reid, W. H., *Hydrodynamic Stability* (Cambridge University Press, 2004).
- ¹²Fjørtoft, R., “Application of integral theorems in deriving criteria of stability for laminar flows and for the baroclinic circular vortex,” *Geophys. Publ.* **17**(6), 1–52 (1950).
- ¹³Gau, C., Shen, C. H., and Wang, Z. B., “Peculiar phenomenon of micro-free-jet flow,” *Phys. Fluids* **21**, 092001 (2009).
- ¹⁴Grek, G., Kozlov, V., and Litvinenko, Y., *Stability of Subsonic Stream Flows and Combustion* (Novosibirsk University Press, 2013) (in Russian).
- ¹⁵Hanel, B. and Richter, E., “Das Verhalten von freistrahlen in verschiedenen Reynolds-zahlbereichen,” *Luft Kältetechnik* **15**(1), 12–17 (1979).
- ¹⁶Howard, L. N., “Note on paper of John W. Miles,” *J. Fluid Mech.* **10**, 509–512 (1961).
- ¹⁷Hussain, A. K. M. F. and Hasan, A. Z., “Turbulence suppression in free turbulent shear flows under controlled excitation. Part 2. Jet-noise reduction,” *J. Fluid Mech.* **150**, 159–168 (1985).
- ¹⁸Jordan, P. and Colonius, T., “Wave packets and turbulent jet noise,” *Annu. Rev. Fluid Mech.* **45**, 173–195 (2013).
- ¹⁹Kambe, T., “The stability of axisymmetric jet with parabolic profile,” *J. Phys. Soc. Jpn.* **26**(2), 566–575 (1969).
- ²⁰Kiwata, T., Usuzawa, T., Komatsu, N., Kimura, S., and Oshkai, P., “Flow structure of a coaxial circular jet with axisymmetric and helical instability modes,” *J. Fluid Sci. Technol.* **6**(4), 437–452 (2011).
- ²¹Koller-Milojević, D. and Schneider, W., “Free and confined jets at low Reynolds numbers,” *Fluid Dyn. Res.* **12**, 307–322 (1993).
- ²²Kozlov, V., Grek, G. R., and Litvinenko, Y., *Visualization of Conventional and Combusting Subsonic Jet Instabilities* (Springer, 2016).
- ²³Kozlov, G., Grek, G., Sorokin, A., and Litvinenko, Y., “Influence of initial conditions at the nozzle exit on the structure of round jet,” *Thermophys. Aeromech.* **15**(1), 55–68 (2008).
- ²⁴Landau, L. D. and Lifshitz, E. M., *Fluid Mechanics* (Pergamon Press, 1959).
- ²⁵Launder, B. E., Morse, A. P., Rodi, W., and Spalding, D. B., “Prediction of free shear flows: A comparison of the performance of six turbulence models,” in *Proceedings of the Conference on Free Turbulent Shear Flows* (NASA, Washington, 1973), Vol. 1, pp. 361–426 (NASA report SP-321).
- ²⁶Lemanov, V. V., Terekhov, V. I., Sharov, K. A., and Shumeiko, A. A., “An experimental study of submerged jets at low Reynolds numbers,” *Tech. Phys. Lett.* **39**(5), 421–423 (2013).
- ²⁷Liang, H. and Maxworthy, T., “An experimental investigation of swirling jets,” *J. Fluid Mech.* **525**, 115–159 (2005).
- ²⁸Lin, C. C., *The Theory of Hydrodynamic Stability* (Cambridge University Press, 1955).
- ²⁹Lipary, G. and Stansby, P. K., “Review of experimental data on incompressible turbulent round jets,” *Flow, Turbul. Combust.* **87**(1), 79–114 (2011).
- ³⁰List, E. J., “Turbulent jets and plumes,” *Annu. Rev. Fluid Mech.* **14**, 189–212 (1982).
- ³¹McNaughton, K. J. and Sinclair, C. G., “Submerged jets in short cylindrical flow vessels,” *J. Fluid Mech.* **25**(2), 367–375 (1966).
- ³²Michalke, A., “Survey on jet instability theory,” *Prog. Aerospace Sci.* **21**, 159–199 (1984).
- ³³Monkewitz, P. A. and Sohn, K. D., “Absolute instability in hot jets,” *AIAA J.* **26**(8), 911–916 (1988).
- ³⁴Morris, P. J., “The spatial viscous instability of axisymmetric jets,” *J. Fluid Mech.* **77**(3), 511–529 (1976).
- ³⁵Morris, P. J., “The instability of high speed jets,” *Int. J. Aeroacoustics* **9**(1), 1–50 (2010).
- ³⁶Navoznov, O. I., Paveliev, A. A., and Yatsenko, A. V., “The transition to turbulence in submerged jets and wakes,” *Fluid Dyn.* **7**(4), 672–678 (1972).
- ³⁷Prandtl, L. and Tietjens, O., *Applied Hydro- and Aeromechanics* (McGraw-Hill, 1934), Vol. 2, p. 22.
- ³⁸Rayleigh, J., *Scientific Papers* (Cambridge University Press, 1892), Vol. 3, p. 575.
- ³⁹Regenscheit, B., “Modellversuche zur erforschung der raumströmung belüfteten räumen,” *Staub* **1**, 14–19 (1964).
- ⁴⁰Reshmin, A., Teplovodskii, S., and Trifonov, V., “Short round diffuser with a high area ratio and a permeable partition,” *Fluid Dyn.* **47**(5), 583–589 (2012).
- ⁴¹Reynolds, A. J., “Observations of a liquid-into-liquid jet,” *J. Fluid Mech.* **14**, 552–556 (1962).
- ⁴²Shtern, V. and Hussain, F., “Effect of deceleration on jet instability,” *J. Fluid Mech.* **480**, 283–309 (2003).
- ⁴³Veser, A., Kuznetsov, M., Fast, G., Friedrich, A., Kotchourko, N., Stern, G., Schwall, M., and Breitung, W., “The structure and flame propagation regimes in turbulent hydrogen jets,” *Int. J. Hydrogen Energy* **36**(3), 2351–2359 (2011).
- ⁴⁴Viluu, A., “An experimental determination of the minimum Reynolds number for instability in a free jet,” *J. Appl. Mech.* **29**(3), 506–508 (1962).
- ⁴⁵Zaitsev, M., Kopiev, V., and Chernyshev, S., “Experimental investigation of the role of instability waves in noise radiation by supersonic jets,” *Fluid Dyn.* **44**, 587–595 (2009).
- ⁴⁶Zaman, K. B. M. Q. and Hussain, A. K. M. F., “Turbulence suppression in free shear flows by controlled excitation,” *J. Fluid Mech.* **103**, 133–159 (1981).